2024 7th International Conference on Soft Robotics (RoboSoft)
San Diego, CA, USA. April 14-17, 2024

Design and Characterization of a Pneumatic Tunable-Stiffness Bellows Actuator

Rongqian Chen, Jun Kwon, Wei-Hsi Chen and Cynthia Sung

Abstract— **We introduce a self-contained pneumatic actuator capable of 1.43 times stiffness gain from 1332 N/m to 1913 N/m without needing an external air source or valve. The design incorporates an air chamber bellows and a spring bellows, connected and sealed. Stiffness modulation is achieved by altering the air chamber volume. We present an approach for computing the volume, pressurized force, and stiffness of a single bellows component, as well as methods for composing single bellows models to predict the change in stiffness of the dual bellows actuator as a function of air chamber compression. We detail the fabrication of the actuator and verify the models on the fabricated prototype. This actuator holds promise for future integration in tunable stiffness robots demanding high strength and adaptability in dynamic scenarios.**

I. Introduction

Soft actuators offer robots flexibility and programmable mechanics, facilitating behaviors such as walking [1], swimming [2], and flying [3]. These actuators frequently demonstrate increased sensitivity [4], agility [3], and adaptability [5], enhancing their capability to generate bio-inspired behaviors and simulate real-life creatures. One valuable feature of soft actuators is the ability to modulate their own stiffness. Robots can alter stiffness for multiple benefits. For example, in legged robots, matching compliance aids in optimizing speed and efficiency [6]. In exoskeletons, adjusting stiffness can modulate energy storage and force generation [7]. Moreover, in soft manipulators, such modifications can provide unique solutions to dexterous manipulation [8], [9].

Common strategies for achieving tunable stiffness can be broadly segregated into two categories: material-based and mechanism-based solutions [10], [11]. A considerable fraction of these tunable stiffness actuator solutions struggle to ensure both precision and quick response. Material-based strategies involve modifying the material's elastic properties through thermal, magnetic, or electric fields, with popular methods including low melting point polymers or alloys [12], shape memory alloys [13], and magnetorheological and electroreheological fluids [10]. Thermal techniques, while achieving large stiffness ranges [10], consume significant energy and introduce challenges for robust control in variable temperature conditions [14]. In contrast, while magnetic and electric approaches exhibit relatively high energy efficiency and swift response [15], their applicability is often constrained by the stiffness range [10]. Mechanical alternatives [9], [16] and fluid-based techniques [17] have garnered recent attention owing to their versatility of design. Among these solutions, pneumatic actuators use pressurized gas, generally through a motorized air pump, to induce motion, and have inherent compliance and sensitivity, rapid actuation, and high power density [18], [15]. However, the sizable pressurized devices and their controllable valves introduce complexity in both design and control [19], [20].

One strategy for building a pneumatic device without air pumps and valves entails using a high-pressure air canister or reservoir as a "battery" to power the mechanical system. For example, Drotman et al. [21] harnessed a CO2 canister to drive electronics-free fluidic control components. Another approach involves mechanically adjusting the volume and valves in conjunction with an air reservoir to pressurize. Liu et al. [22] used this technique on a tendon-driven origami pump actuator and Wang et al. [23] in a dual bellows actuated gripper. Such systems do not need a continuous air pump to control pressure. Our work builds upon this closed reservoir approach and provides an actuator model.

In this paper, we introduce a dual-bellows pneumatic actuator capable of adjusting stiffness by over 1.43 times within a closed system powered by a DC motor. The actuator's system pressure and spring bellows' stiffness are governed by the compression of the air chamber bellows, with the pressure and output force controlled by a motor-driven mechanism, as depicted in Fig. 1. An internal pressure sensor enables stiffness monitoring. We introduce a mathematical model for the relationship between the air chamber compression and output stiffness. The primary contributions of this paper are:

- a pneumatic tunable-stiffness actuator mechanism free of air pumps or valves
- whose states can be monitored through embedded sensing, allowing for control over the output force, and
- mathematical models predicting volume, pressure, and force output, with errors less than $1.5\,\mathrm{mL}$ in volume and $2\,\mathrm{N}$ in force.

The remainder of this paper is organized as follows. Section II describes the design of the actuator and its operational mechanisms. Section III outlines and verifies the mathematical model governing the volume, pressure, and force in a single pneumatic bellows actuator. Section IV adapts the previously proposed model for a single bellows to a dual bellows actuator. Finally, Section V describes potential applications and future prospects of this research.

Support for this project has been provided in part by NSF Grant No. 1845339 and by the Army Research Office (ARO) under MURI award #W911NF1810327.

R. Chen, J. Kwon, W.-H. Chen and C. Sung are with the General Robotics, Automation, Sensing & Perception (GRASP) Lab at the University of Pennsylvania, Philadelphia, PA, USA. (e-mail: {willchan, junkwon, weicc, crsung}@seas.upenn.edu)

2024 IEEE 7th International Conference on Soft Robotics (RoboSoft) | 979-8-3503-8181-8/24/$31.00 ©2024 IEEE | DOI: 10.1109/ROBOSOFT60065.2024.10521916

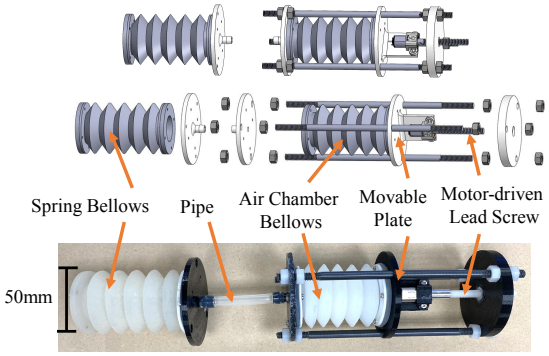

Fig. 1. Dual-bellows actuator design. Top: Assembled actuator. Middle: Exploded view with parts labeled. Bottom: Actuator prototype.

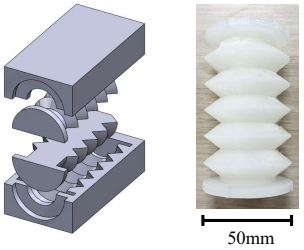

Fig. 2. Left: Bellows mold. Right: Molded bellows.

II. Tunable-Stiffness Bellows Design and Fabrication

A. Design Overview and Fabrication

The tunable-stiffness actuator consists of two interconnected soft pneumatic bellows, an enclosed air chamber (functions as the air reservoir), and a spring (functions as the actuator), as depicted in Fig. 1. In contrast to traditional pneumatic actuators, which rely on air pumps for actuation, our approach uses an electric motor to adjust the volume of the soft actuator and alter its mechanical properties. The system maintains an airtight seal, allowing us to use volume changes in the air chamber to change the internal pressure of the system and thus the stiffness of the spring bellows. A motor-driven lead screw mechanism regulates the air chamber's volume. The non-back-drivable lead screw also "locks" the configuration of the air chamber, which does not need energy to maintain its current stiffness.

To construct the system, two bellows are molded from silicone rubber (Smooth-on MoldStar 31T). The mold is separated into two pieces, with two halves of each bellows cast as symmetrical segments. After the two halves are cured and the cores removed, they are aligned, fixed with a clamp, and bonded by a thin layer of the same silicone rubber. The two bellows are attached to rigid 3D plates at both ends using screws and sealed using the same silicone. The plates are printed with rectilinear infill at a 100% infill rate to ensure air-tightness. Additionally, XTD-3D coating material is applied to the connection plate, filling surface gaps. The two bellows are connected to each other via rubber tubing and barbed hose connectors. We tested the airtightness of the actuator and show that the pressure decrease is only 1% after more than 100 cycles of compression and release.

To control the stiffness of the spring bellows, the volume of the air chamber bellows is modulated by controlling a movable plate on a 20 threads per inch lead screw. This screw is driven by a Pololu DC motor with a gear ratio of 100:1 and a magnetic encoder for position tracking. To ensure linear motion, the plate is guided by three rods. The compression of the air chamber is controlled using PD control.

B. Design Parameters

The bulk stiffness and the achievable stiffness range of the actuator depend on a number of design parameters, detailed in Table I. The primary challenge in the design process lies in the careful selection of values for these parameters to ensure the actuator functions within the desired scale, maximizes its tunable stiffness range, and avoids unwanted mechanical failures, such as buckling. Notably, geometric factors, including wall thickness, length (as influenced by the number of segments), and the volumes of the two chambers, directly impact the stiffness and its adjustable range. Simultaneously, the design must address the length-to-width ratio (slenderness) and the ratio of the outer and inner radius of the soft bellows to prevent buckling. Additionally, material properties play a significant role in the overall performance.

Initially, we established the appropriate scale for the actuator, taking into account our intended application, which involves eventual integration into a mesoscale dynamic robot similar to the REBO hopper [24]. As a starting point, we set the rest length of the spring bellows to $90.3\,\mathrm{mm}$.

Subsequently, through a systematic process of trial and error, we identified the parameters that yielded the best performance among samples we fabricated, as outlined in Table II. Both bellows are designed with matching cone angles and number of segments. The spring bellows operates without guided rods and experiences larger deformations than the air chamber, so we increase the spring bellows wall thickness by $1\,\mathrm{mm}$ to maintain structural integrity. As the air chamber compresses, air pressure naturally increases. However, under high-pressure conditions, the bellows can deform uncontrollably. To mitigate this issue, we have chosen to set the system volume to atmosphere pressure when the air chamber bellows is compressed to $20\,\mathrm{mm}$ so the system pressure will be lower than atmosphere pressure when compression is less than $20\,\mathrm{mm}$. Although this approach reduces the maximum air pressure, and consequently the maximum reachable stiffness, the offset in pressure prevents the bellows from buckling. This results in enhanced controllability and a broader range of tunable stiffness. Furthermore, this method proves effective in minimizing air leakage. Given potential fabrication defects, even minor gaps can cause significant pressure drops under high-pressure conditions.

III. Single Bellows Model and Characterization

In order to analyze the ability of the pneumatic bellows to generate real-time tunable stiffness, we derive the relationships between the volume, pressure, force, and compression.

Each bellows can be modeled as a concatenation of identical segments, where each segment is formed of two conical frusta of opposite orientation, as shown in Fig. 3. The

TABLE I

EFFECTS OF MODIFYING BELLOWS PROPERTIES

Design Property	Effect when Increased	Effect when Decreased
Wall thickness	Reduce stiffness range	Wall bulging/Buckling
Segment numbers	Bending and instability	Lower action length
Air chamber volume	Increase stiffness range	Reduce stiffness range
Spring chamber volume	Reduce stiffness range	Increase stiffness range
Length-to-width ratio	Bending	Not significant
Outer-to-inner radii ratio	Bending/Wall collision	Buckling
Young's Modulus	Reduce stiffness range	Uneven deformation
Internal pressure	Wall expansion/Buckling	Adjacent wall collision

TABLE II

BELLOW PARAMETERS

Bellows Type	R (mm)	r (mm)	t (mm)	h (mm)	n
Air Chamber	20.1	10.58	3	14.92	5
Spring	18.47	9	4	14.92	5

bellows has segment count n, segment height h, large radius R, and small radius r. The wall thickness of the bellows is t. The internal volume of the bellows is denoted as V, and the internal air pressure is P. We denote the initial state of the bellows using a subscript 0. Thus, the initial height of a segment is h_0, and the initial volume and internal pressure of the bellows are V_0 and P_0, respectively.

When the bellows compresses or elongates, we assume that each segment deforms equally so that the individual segment displacement is denoted by a single variable $\Delta h = h_0 - h$. As the bellows deforms, the volume and internal pressure change, so V and P are functions of Δh.

A. Pressure

The internal pressure of the bellows is related to its volume through the Ideal Gas Law as

$$P(\Delta h)V(\Delta h) = P_0 V_0. \tag{1}$$

In this case, the pressure in the bellows can be determined uniquely by measuring the volume, and vice versa.

B. Volume

1) Geometric Volume: In order to determine how the volume of the bellows changes with compression, we start with a geometric analysis. Assume that the small radius r remains constant while the large radius $R(\Delta h)$ changes. Then, the large radius can be computed by solving the following equation [23]:

$$(R(\Delta h) - r)^2 + \frac{(h_0 - \Delta h)^2}{4} = (R_0 - r)^2 + \frac{h_0^2}{4}, \tag{2}$$

resulting in

$$R(\Delta h) = \sqrt{(R_0 - r)^2 - \frac{\Delta h^2 - 2h_0\Delta h}{4}} + r. \tag{3}$$

The volume of the bellows can then be computed as the combined volume of $2n$ conical frustra with radius r and $R(\Delta h)$ and height $h/2$:

$$V_{geo}(\Delta h) = \frac{1}{3}\pi n(h_0 - \Delta h)\left(R(\Delta h)^2 + r^2 + R(\Delta h)r\right) \tag{4}$$

Note that for this idealized model, we assume that the wall thickness remains constant and that the volume at the point of connection between the chamber and the spring is negligible.

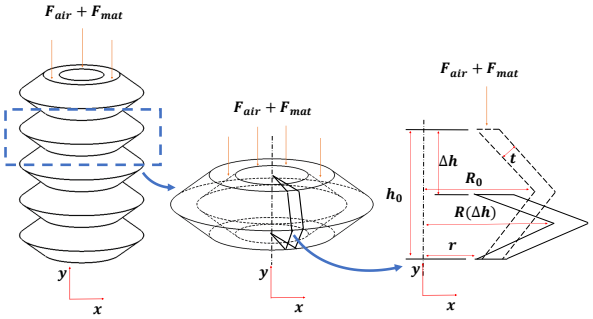

Fig. 3. Bellows geometric model.

2) Augmented Volume Model: The geometric model assumes that the walls experience no warping. However, in practical scenarios, the wall does exhibit deflection upon compression even under no air pressure. During physical experiments, we noticed that the wall bulged outward as the compression increased. To precisely characterize the non-linear change in volume due to wall warping, we thus augment the geometric model with a data-driven model.

To evaluate the quality of the geometric model and conduct a fit of the error, we performed experiments measuring the volume of the bellows under different amounts of compression and pressurization. The experimental setup is detailed in Fig. 4. The displacement of the bellows is controlled by a motor-driven lead screw sliding along guide rods. The bellows is connected to a non-deformable syringe via rubber tubing. The syringe is manipulated to set the system's initial pressure. A pressure sensor, connected to the tubing through a tee-shaped connector, monitors the pressure over time.

We measured the pressure inside the bellows for different starting pressures and compression amounts. In particular, the syringe was exposed to the atmosphere and the plunger was set to produce a particular internal volume. The syringe was then reconnected to the system and the plunger was repositioned so that the syringe volume returned to the pairing bellows' volume. This ensured that every test began with a consistent system volume, albeit under varying pressures. The bellows was then compressed while recording the internal pressure of the system. The pressures were converted into volumes using the Ideal Gas Law. Measurements were taken when the syringe plunger position under atmosphere pressure ranged from $-15\,\mathrm{mm}$ to $15\,\mathrm{mm}$ with an increment of $5\,\mathrm{mm}$, where $0\,\mathrm{mm}$ position syringe volume corresponds to the uncompressed pairing bellows' volume. During measurements, the air chamber bellows pressure ranged from $88\,970\,\mathrm{Pa}$ to $112\,120\,\mathrm{Pa}$, and the spring bellows pressure ranged from $87\,860\,\mathrm{Pa}$ to $113\,840\,\mathrm{Pa}$. Bellows compressions were tested from $0\,\mathrm{mm}$ to $30\,\mathrm{mm}$ with an increment of $5\,\mathrm{mm}$. Two bellows samples were tested, corresponding to

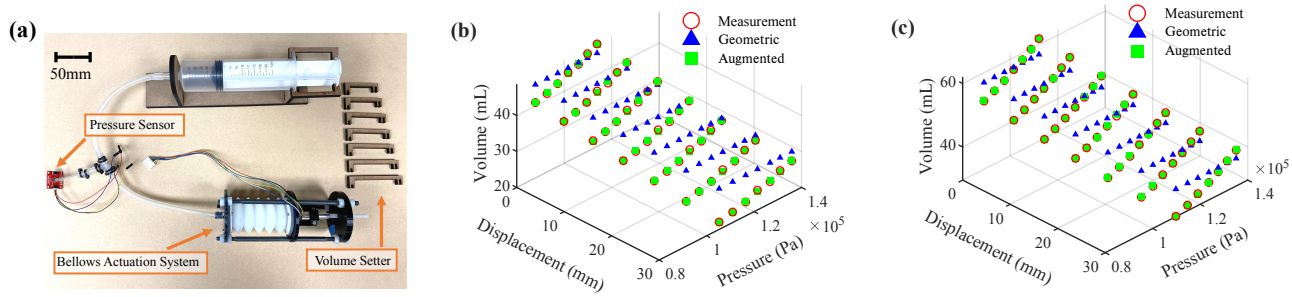

Fig. 4. Bellows volume test. (a) Syringe bellows test setup. Comparison between the bellows volume measure and the two prediction models, Eq. (4) and (6) for (b) the spring bellows, and (c) the air chamber bellows.

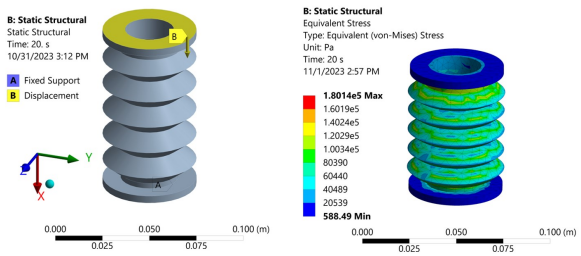

Fig. 5. Ansys static structural simulation. Left: Undeformed bellows model with supports and compression indicated. Right: Simulated model at max compression, colored according to local stress.

the design parameters in Table II.

Fig. 4 compares the geometric model prediction in blue triangles and the experimental measurements in red circles. The data shows clear changes along both the pressure and compression dimensions, indicating that the pressure deforms the soft material of the bellows.

In order to capture this trend, we conduct a least squares fit of the volumetric error to a cubic polynomial of the form:

$$\begin{aligned} E_V(\Delta h, P) &= a_{00} + a_{10}\Delta h + a_{01}P \\ &+ a_{20}\Delta h^2 + a_{11}\Delta hP + a_{02}P^2 \\ &+ a_{30}\Delta h^3 + a_{21}\Delta h^2 P + a_{12}\Delta hP^2 + a_{03}P^3, \end{aligned} \tag{5}$$

where E_V is the volumetric error and a_{ii} are fitting coefficients. The volume $V(\Delta h, P)$ is then the sum of the geometric model and this polynomial error correction function:

$$V(\Delta h, P) = V_{geo}(\Delta h) + E_V(\Delta h, P). \tag{6}$$

Fig. 4 also displays the augmented model in green squares. The augmented volume model reduces error by accounting for wall bulging volume change caused by the air pressure and material softness, and matches the measurement to within $0.4\,\mathrm{mL}$.

C. Force

The reaction force produced by the bellows under compression consists of two components. The first component is the pressure-induced force, which is a function of both the air pressure within the bellows and the displacement of the bellows. The second component is the material-induced force which is contingent upon the structural design and the materials. We can compute the total force, then, as the sum

$$F(\Delta h, P) = F_{air}(\Delta h, P) + F_{mat}(\Delta h, P). \tag{7}$$

1) Pressure-Induced Force: Suppose that the system has no energy loss and temperature variation during the shape change, the work done by the gas displacing the bellows by an infinitesimal distance dh is

$$dW = F_{air}d(nh) = (P - P_{atm})dV, \tag{8}$$

where F_{air} is the external force required to generate the displacement Δh, P_{atm} =101 325 Pa is atmospheric pressure of the air surrounding the bellows, and dV is the differential volume of the gas. The force generated by the internal pressure F_{air} is then:

$$F_{air}(\Delta h, P) = (P(\Delta h) - P_{atm})\,\frac{dV(\Delta h)}{d(nh)}. \tag{9}$$

The value $dV/d(nh)$ can be regarded as the equivalent cross-sectional area of the bellows. Using the volume model from Sec. III-B, this quantity can be calculated as

$$\begin{aligned} \frac{dV}{d(nh)} &= \frac{dV_{geo}(\Delta h)}{ndh} + \frac{dE_V(\Delta h, P)}{ndh} \\ &= \frac{\pi}{3}\left(R(\Delta h)^2 + r^2 + R(\Delta h)r\right) + \frac{dE_V(\Delta h, P)}{ndh}. \end{aligned} \tag{10}$$

2) Material-Induced Force: To estimate the component of force that is produced through material compression, we conduct an FEA simulation using Ansys. The silicone rubber used for experiments has a Young's modulus of $0.9\,\mathrm{MPa}$, measured by an MTS Criterion (Series 40) machine, whose test probe was set to compress $20\,\mathrm{mm}$ with a velocity of $1\,\mathrm{mm/s}$. The measured density is $1046\,\mathrm{kg/m^3}$. We approximate the Poisson's ratio as 0.49. We choose a meshing size of $0.25\,\mathrm{mm}$. Fig. 5 depicts the simulation configuration: the bottom plate is fixed while the top plate undergoes compression along the x-axis up to a distance of $20\,\mathrm{mm}$ with a velocity of $1\,\mathrm{mm/s}$. Fig. 5(b) shows a snapshot of the simulation under maximum compression of $20\,\mathrm{mm}$. Each segment shows a similar stress profile to all the others.

The resulting force-displacement curve for the spring bellows is shown in Fig. 7, compared to measurements taken on the MTS machine for the bellows structure in an unpressurized state. In general, the results exhibit good alignment with measured force output and the maximum error is 6.4%. The deviation increases with increasing compression, and may be due to increased wall bulging effect.

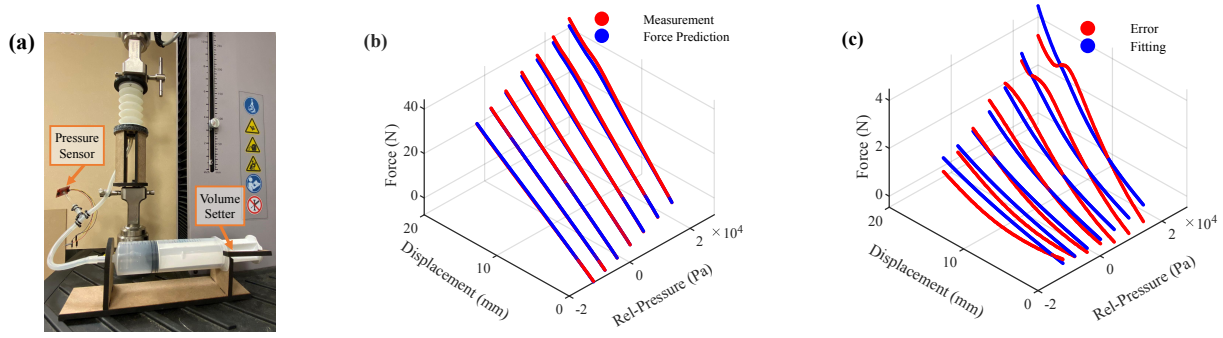

Fig. 6. The single bellows mechanical test: (a) Syringe bellows MTS test setup. (b) Spring bellows force comparison between measurement and prediction. Relative pressure represents the pressure after subtracting the offset of atmospheric pressure. (c) Spring bellows force prediction error and fitting function.

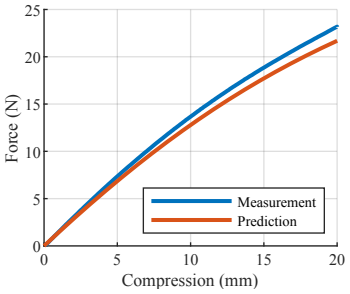

Fig. 7. Force-displacement curve of unpressurized bellows as predicted by FEA simulation, compared to experimental MTS measurements.

3) Augmented Material-Induced Force: Similarly to how the volume model changes with the internal pressure, the force produced by the material of the bellows structure changes when the bellows is pressurized. This is because the internal pressure causes bulging or collapse of the bellows walls, which affects their geometry and the local stresses in the system. We thus also add an error correction term to the material model. Unfortunately, it is difficult to measure the material stresses of a pressurized bellows without actually pressurizing the bellows. Thus, we take experimental measurements of the total force of produced when pressurizing and compressing a bellows structure and use this data to fit an error model to the material-induced force.

The experimental setup for these tests is the same as that used for volume measurements in Sec. III-B.2, except that the force was logged on the MTS system. The MTS test parameters are the same as Sec. III-C.2. The results for the spring bellows are shown in Fig. 6. For comparison, the force prediction when computed using Eq. (7) and assuming that the MTS measurements completely characterize the force produced when compressing the material are also shown.

Since the results display increasing prediction error for increasing internal pressures and displacements, we introduce an additional exponential fitted error term of the form

$$E_F(\Delta h, P) = C_1 e^{C_2 P + C_3 \Delta h + C_4}. \tag{11}$$

The equation includes force error as a function of internal pressure and bellows displacement. The plot of this function is depicted in Fig. 6 (c) in blue. In general, the trends in the fitting function match those of the error. Buckling occurs when the bellows is subjected to large pressure and compression, increasing fitting error.

The augmented material-induced force prediction is then

$$F_{mat} = F_{MTS}(n\Delta h) + E_F(\Delta h, P), \tag{12}$$

which consists of an FEA simulated term F_{MTS} and an error E_F determined by both pressure and displacement. The model matches the measured forces except at high pressure and displacement conditions, where buckling occurs.

D. Stiffness

Given the force response of the bellows, the stiffness can then be calculated as

$$K(\Delta h, P) = \frac{d}{d(\Delta h)} F(\Delta h, P) \tag{13}$$

and is a function of both the displacement and the pressure.

IV. Dual Bellows Stiffness Control

Because the stiffness of a single bellows changes with internal pressure and internal pressure changes with volume, two bellows can be connected in series to form a tunable-stiffness actuator, as described in Sec. II. We show how the single bellows models can be composed to predict stiffness change and validate these models on our fabricated design.

A. Model

Consider two bellows connected in series: an air chamber and a spring. To model the combined structure, we characterize the volume, pressure, and force changes in the spring as a function of air chamber compression.

Let the subscript c denote any variables related to the air chamber and the subscript s denote variables related to the spring. Each of the bellows in this system individually follows the model described in Sec. III-B.2. That is,

$$V_c(\Delta h_c, P_c) = V_{geo,c}(\Delta h_c) + E_{V,c}(\Delta h_c, P_c) \tag{14}$$
$$V_s(\Delta h_s, P_s) = V_{geo,s}(\Delta h_s) + E_{V,s}(\Delta h_s, P_s) \tag{15}$$

Further, when the two bellows are connected, air is shared between them, so the system is subject to the constraint

$$P_s = P_c = P \tag{16}$$

that is, the air pressure is uniform throughout the entire system. The full system must satisfy the Ideal Gas Law:

$$\begin{aligned} P\left(V_s(\Delta h_s, P) + V_c(\Delta h_c, P) + V_{tube}\right) \\ = P_0(V_{s0} + V_{c0} + V_{tube}), \end{aligned} \tag{17}$$

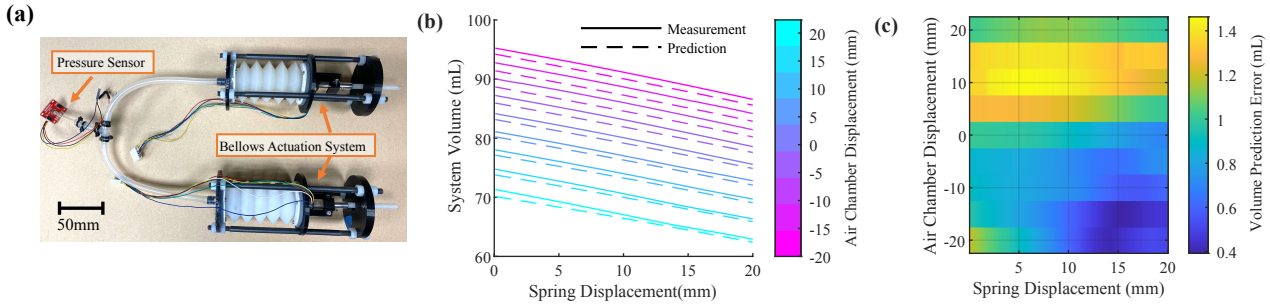

Fig. 8. Dual bellows volume test: (a) Test setup. (b) Comparison between measured and predicted volume. (c) Error in augmented volume model.

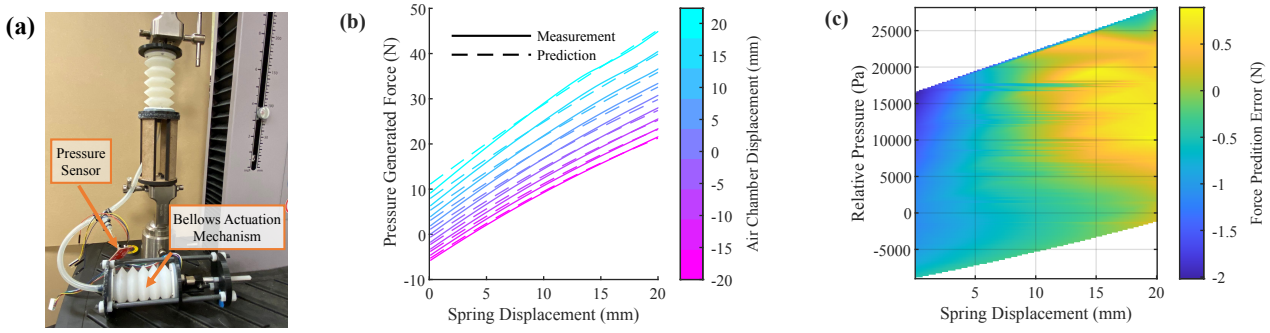

Fig. 9. Dual bellows mechanical test: (a) MTS test setup. (b) Comparison between measured and predicted force. (c) Error in augmented force model.

where V_{tube} is the volume of the tube connecting the two bellows and is a constant.

Solving this system of equations indicates that the pressure P and the volumes V_c and V_s of the bellows can be computed directly as a function of the bellows displacements Δh_c and Δh_s. Further, by substituting the computed pressure P into Eq. (7) for the spring reaction force $F_s(\Delta h_c, P)$, we find that the reaction force can also be computed strictly as a function of the bellows displacement, i.e. $F_s = F_s(\Delta h_c, \Delta h_s)$, and so can the stiffness $K_s(\Delta h_c, \Delta h_s)$.

B. Experimental Validation

To verify that the bellows models can indeed be composed in this way, we conduct the same tests on a dual bellows test setup, which consists of a spring bellows and an air chamber bellows, as shown in Fig. 8 (a). Both bellows are controlled by motor-driven lead screws and a pressure sensor is connected to track the internal pressure over time. The pressure signal is converted into volume using the Ideal Gas Law. The air chamber bellows was compressed to displacements from $-20\,\mathrm{mm}$ to $20\,\mathrm{mm}$ in increments of $5\,\mathrm{mm}$, and spring bellows was compressed continuously from $0\,\mathrm{mm}$ to $20\,\mathrm{mm}$ while tracking pressure. Fig. 8 (b) and (c) show the resulting measurements compared to the model prediction. All the prediction errors are between $0.4\,\mathrm{mL}$ and $1.5\,\mathrm{mL}$ and might be attributable to inaccuracies in system volume measurement and tiny air leakage.

For measuring the force response, the setup is placed in the MTS machine as shown in Fig. 9. The reaction force is measured directly as a function of spring compression when the air chamber is compressed to set amounts of $-20\,\mathrm{mm}$ to $20\,\mathrm{mm}$ with an increment of $5\,\mathrm{mm}$. Fig. 9 (b) and (c) depict the results compared to the force predicted by the model.

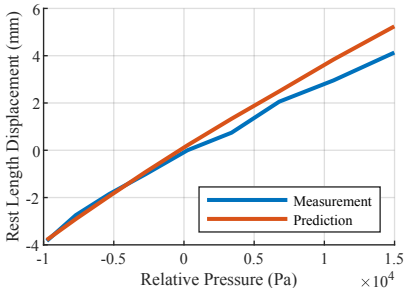

Fig. 10. Rest length elongation as a function of internal pressure, as predicted by the model and measured experimentally.

Predictions are all within $-2\,\mathrm{N}$ to $1\,\mathrm{N}$ of the measured values, indicating good agreement.

C. Elongation and Contraction

In practical applications, the bellows's natural length changes when it is pressured. In particular, it contracts when the internal pressure is below atmospheric levels and expands when the internal pressure surpasses atmospheric levels. Fig. 10 shows the predicted change in rest length for the spring bellows as a function of internal pressure. The forecasted results align well with the expectations at low pressure below atmospheric pressure while working less effectively at high pressures because of buckling.

D. Achievable Stiffness

The force curves in Fig. 6 (c) have slopes that increase with the air chamber displacement, verifying that the stiffness can be changed. To estimate the stiffness of the actuator, we consider the spring displacement range from $0\,\mathrm{mm}$ to $12\,\mathrm{mm}$ and compute the average slope of the force curve in this region. The result is a stiffness of $1483\,\mathrm{N/m}$ at a low air chamber displacement of $-20\,\mathrm{mm}$ and a stiffness of

$1975\,\mathrm{N/m}$ at a high air chamber displacement of $20\,\mathrm{mm}$, corresponding to a stiffness range of approximately 1.33 times. This experimentally achieved stiffness range is greater than the model-predicted stiffness range of $1458\,\mathrm{N/m}$ to $1758\,\mathrm{N/m}$ (a change of about 1.2 times).

Note that the force curves are nonlinear, and that the stiffness is higher at low displacements. Extending the curves out to the spring bellows' extended rest length, we find a larger achievable stiffness range of between $1332\,\mathrm{N/m}$ and $1913\,\mathrm{N/m}$ (1.43 times) from when the air chamber is fully elongated to when it is fully compressed by $48.0\,\mathrm{mm}$. The curves exhibit buckling under high pressure.

V. Conclusion

In this paper, we have developed a pneumatic bellows actuator with tunable stiffness capabilities. The actuator consists of two bellows chambers connected together, where deformation of the air chamber bellows induces stiffness changes in the spring bellows. The actuator is self-contained, requiring no external pressure sources, and is actuated using an electromechanical DC motor with standard off-the-shelf electronics. A description of the proposed design and the fabrication process is provided. We also present a model for predicting the volume, pressure, force, and stiffness change of a single bellows as it is deformed. While geometric models can capture most of the bellow's behavior, the soft walls of the bellows bulge under pressurization that must be fitted to data. We also demonstrate how to compose single bellows models to capture the response of the dual-bellows system.

While our models are able to capture the behavior of the fabricated bellows structure, a large number of experiments are needed to characterize the volume and force output and account for bulging in the soft material. In the future, further characterization is required to optimize the bellows design to maximize stiffness range and to improve stability and robustness against buckling and other instabilities.

The actuator is able to achieve relatively high stiffnesses in the $1332\,\mathrm{N/m}$ to $1913\,\mathrm{N/m}$ range, with a 1.43 times stiffness gain. Because of these properties, we expect that the actuator can be used in dynamic robots applications similar to [24]. The system is able to store energy and maintain its stiffness passively, with output based on the air chamber compression, which can be sensed using an encoder and controlled by the motor. Future work includes incorporating this bellows into a hopping robot to test its ability to withstand repeated high-impact loading typical of these sorts of dynamical tasks, and to analyze how tunable stiffness can be used for more efficient locomotion and adaptation.

References

[1] M. Calisti, G. Picardi, and C. Laschi, "Fundamentals of soft robot locomotion," *Journal of The Royal Society Interface*, vol. 14, no. 130, p. 20170101, 2017.

[2] R. K. Katzschmann, A. D. Marchese, and D. Rus, "Hydraulic autonomous soft robotic fish for 3D swimming," in *International Symposium on Experimental Robotics*, 2015, pp. 405–420.

[3] H. V. Phan and H. C. Park, "Insect-inspired, tailless, hover-capable flapping-wing robots: Recent progress, challenges, and future directions," *Progress in Aerospace Sciences*, vol. 111, p. 100573, 2019.

[4] R. Baines, F. Zuliani, N. Chennoufi, S. Joshi, R. Kramer-Bottiglio, and J. Paik, "Multi-modal deformation and temperature sensing for context-sensitive machines," *Nature Communications*, vol. 14, no. 1, p. 7499, 2023.

[5] R. Baines, S. K. Patiballa, J. Booth, L. Ramirez, T. Sipple, A. Garcia, F. Fish, and R. Kramer-Bottiglio, "Multi-environment robotic transitions through adaptive morphogenesis," *Nature*, vol. 610, no. 7931, pp. 283–289, 2022.

[6] K. C. Galloway, J. E. Clark, M. Yim, and D. E. Koditschek, "Experimental investigations into the role of passive variable compliant legs for dynamic robotic locomotion," in *IEEE International Conference on Robotics and Automation*, 2011, pp. 1243–1249.

[7] T. Zhang and D. J. Braun, "Human driven compliant transmission mechanism," in *IEEE International Conference on Robotics and Automation (ICRA)*, 2021, pp. 7094–7099.

[8] B. Zhao, L. Zeng, Z. Wu, and K. Xu, "A continuum manipulator for continuously variable stiffness and its stiffness control formulation," *Mechanism and Machine Theory*, vol. 149, p. 103746, 2020.

[9] N. G. Cheng, M. B. Lobovsky, S. J. Keating, A. M. Setapen, K. I. Gero, A. E. Hosoi, and K. D. Iagnemma, "Design and analysis of a robust, low-cost, highly articulated manipulator enabled by jamming of granular media," in *IEEE International Conference on Robotics and Automation*, 2012, pp. 4328–4333.

[10] M. Manti, V. Cacucciolo, and M. Cianchetti, "Stiffening in soft robotics: A review of the state of the art," *IEEE Robotics & Automation Magazine*, vol. 23, no. 3, pp. 93–106, 2016.

[11] F. Ahmed, M. Waqas, B. Jawed, A. M. Soomro, S. Kumar, A. Hina, U. Khan, K. H. Kim, and K. H. Choi, "Decade of bio-inspired soft robots: A review," *Smart Materials and Structures*, vol. 31, no. 7, p. 073002, 2022.

[12] W. Shan, T. Lu, Z. Wang, and C. Majidi, "Thermal analysis and design of a multi-layered rigidity tunable composite," *International Journal of Heat and Mass Transfer*, vol. 66, pp. 271–278, 2013.

[13] D. Niu, D. Li, J. Chen, M. Zhang, B. Lei, W. Jiang, J. Chen, and H. Liu, "Sma-based soft actuators with electrically responsive and photoresponsive deformations applied in soft robots," *Sensors and Actuators A: Physical*, vol. 341, p. 113516, 2022.

[14] S. Kim, C. Laschi, and B. Trimmer, "Soft robotics: a bioinspired evolution in robotics," *Trends in Biotechnology*, vol. 31, no. 5, pp. 287–294, 2013.

[15] J. Zhang, J. Sheng, C. T. O'Neill, C. J. Walsh, R. J. Wood, J.-H. Ryu, J. P. Desai, and M. C. Yip, "Robotic artificial muscles: Current progress and future perspectives," *IEEE Transactions on Robotics*, vol. 35, no. 3, pp. 761–781, 2019.

[16] S. Misra, M. Mitchell, R. Chen, and C. Sung, "Design and control of a tunable-stiffness coiled-spring actuator," in *IEEE International Conference on Robotics and Automation (ICRA)*, 2023, pp. 634–640.

[17] Y. Liu, Y. Yang, Y. Peng, S. Zhong, N. Liu, and H. Pu, "A light soft manipulator with continuously controllable stiffness actuated by a thin mckibben pneumatic artificial muscle," *IEEE/ASME Transactions on Mechatronics*, vol. 25, no. 4, pp. 1944–1952, 2020.

[18] M. S. Xavier, C. D. Tawk, A. Zolfagharian, J. Pinskier, D. Howard, T. Young, J. Lai, S. M. Harrison, Y. K. Yong, M. Bodaghi, *et al.*, "Soft pneumatic actuators: A review of design, fabrication, modeling, sensing, control and applications," *IEEE Access*, vol. 10, pp. 59 442–59 485, 2022.

[19] D. Rus and M. T. Tolley, "Design, fabrication and control of soft robots," *Nature*, vol. 521, no. 7553, pp. 467–475, 2015.

[20] H. Jiang, Z. Wang, Y. Jin, X. Chen, P. Li, Y. Gan, S. Lin, and X. Chen, "Hierarchical control of soft manipulators towards unstructured interactions," *The International Journal of Robotics Research*, vol. 40, no. 1, pp. 411–434, 2021.

[21] D. Drotman, S. Jadhav, D. Sharp, C. Chan, and M. T. Tolley, "Electronics-free pneumatic circuits for controlling soft-legged robots," *Science Robotics*, vol. 6, no. 51, p. eaay2627, 2021.

[22] Y. Kim, Y. Lee, and Y. Cha, "Origami pump actuator based pneumatic quadruped robot (oparo)," *IEEE Access*, vol. 9, pp. 41 010–41 018, 2021.

[23] L. Wang and Z. Wang, "Mechanoreception for soft robots via intuitive body cues," *Soft Robotics*, vol. 7, no. 2, pp. 198–217, 2020.

[24] W.-H. Chen, S. Misra, J. D. Caporale, D. E. Koditschek, S. Yang, and C. R. Sung, "A tendon-driven origami hopper triggered by proprioceptive contact detection," in *IEEE International Conference on Soft Robotics (RoboSoft)*, 2020, pp. 373–380.